Available online at www.sciencedirect.com
SCIENCE DIRECT®
Journal of Power Sources 115 (2003) 305–314
JOURNAL OF POWER SOURCES
www.elsevier.com/locate/jpowsour

Effects of aluminum on the structural and electrochemical properties of $LiNiO_2$

M. Guilmard, A. Rougier, M. Grüne, L. Croguennec*, C. Delmas

Institut de Chimie de la Matière Condensée de Bordeaux-CNRS and Ecole Nationale Supérieure de Chimie et Physique de Bordeaux, Université Bordeaux I, 87, Av. Dr A. Schweitzer, 33608 Pessac Cedex, France

Received 9 October 2002; accepted 16 December 2002

Abstract

$LiNi_{1-y}Al_yO_2$ ($0.10 \leq y \leq 0.50$) compounds have been synthesized by a coprecipitation method. The characterization of the samples by X-ray and neutron diffraction, associated with Rietveld refinement analysis, has shown that for all materials, about 5% extra-nickel ions are present in the interslab space. Charge–discharge cycling of $LiNi_{1-y}Al_yO_2$ as positive electrode material in lithium cells has shown that aluminum substitution suppresses all the phase transitions observed for the $LiNiO_2$ system. Good cycling stability was observed, but the capacity decreases from 125 to 100 mAh/g by increasing the aluminum amount from 10 to 25% (3–4.15 V range; *C*/20 rate).

Keywords: Intercalation; Lithium battery; $LiNiO_2$; Aluminum substitution; Diffraction

1. Introduction

With the development of lithium-ion batteries, many studies have been devoted to $LiNiO_2$. Indeed, this layered material presents higher potentialities, compared to the present commercialized $LiCoO_2$, in terms of reversible capacity and cost [1–5]. Nevertheless, due to the non negligible vapor pressure of lithium oxide at the calcination temperature and to the difficulty to oxidize Ni^{2+} to Ni^{3+} ions, $LiNiO_2$ compounds are generally lithium deficient with the presence of z extra-nickel ions in the lithium site, leading thus to the formula $Li_{1-z}Ni_{1+z}O_2$. This lithium deficiency is highly dependent on the synthesis conditions and has severe effects on the electrochemical properties [6–8]. Indeed, it induces loss of reversibility at the end of the first discharge due to the irreversible oxidation of extra-nickel ions during the first charge, that leads to an irreversible shrinkage of the interslab space [8,9]. Problem of capacity fading is observed upon long term cycling [5]. Moreover, thermal instability of highly deintercalated Li_xNiO_2 compounds could lead to severe safety problems and is, therefore, a major concern for battery manufacturers [10–12].

Partial substitutions for nickel were studied in order to improve the material properties. In particular, a decrease of extra-nickel ions amount in the interslab space is obtained by cobalt substitution [13–17]. Substitution of Mg [18], Ga [19], Nb [20], Ca [20], etc. for nickel limits the capacity fading. Differential scanning calorimetry measurements show the positive effect of Al [11,21], Mn [22,23], Ti [22,24], Mg/Ti [25], etc. substitutions for nickel to improve the thermal stability.

Up to now, partial aluminum substitution for nickel seems to be the most promising for thermal stabilization of $LiNiO_2$ [11,21]. $LiNi_{1-y}Al_yO_2$ system was previously studied by Rougier [26], Ohzuku [11], Zhong [27] and Wang [28], the aluminum-substituted materials having been synthesized by solid state reaction. More recently, Park studied $LiNi_{1-y}Al_yO_2$ compounds obtained by a sol–gel method [29]. A solid solution was obtained up to 20% aluminum substitution for nickel by Rougier [26] and Zhong [27], 25% by Wang [28] and 50% by Ohzuku [11]. The structural characterization performed by Rougier and Ohzuku [11,26] has shown that aluminum substitution suppresses all the phase transitions observed upon cycling for the Li_xNiO_2 system. Furthermore, aluminum substitution for nickel was also shown to improve the cycle life [21,26,29] of the $Li//LiNi_{1-y}Al_yO_2$ system, and to reduce the capacity fading [29]. Nevertheless, a significant decrease of the reversible capacity with an increase of Al content was also observed, due to the electrochemical inactivity of the substituant during the redox process [27–29].

* Corresponding author. Tel.: +33-5-5796-2234; fax: +33-5-5684-6698.
E-mail address: crog@icmcb.u-bordeaux.fr (L. Croguennec).

0378-7753/03/$ – see front matter
doi:10.1016/S0378-7753(03)00012-0

The $LiNi_{1-y}Al_yO_2$ phases ($0.10 \leq y \leq 0.50$) presented in this paper were synthesized by the coprecipitation method, in order to try to obtain better homogeneity of the materials. A large part of this work concerns the structural characterization of the starting compounds that was not performed in detail in the previous studies. Electrochemical performances were also studied, associated with a structural characterization of the deintercalated phases. In a forthcoming paper, the thermal behavior of the deintercalated phases will be presented in detail.

2. Experimental

$LiNi_{1-y}Al_yO_2$ ($0.10 \leq y \leq 0.50$) phases were synthesized by a coprecipitation method in aqueous solution as described by Caurant et al. [30]. A 1 M aqueous solution of $Ni(NO_3)_2$ and $Al(NO_3)_3$ prepared with the $(1-y)/y$ molar ratio was added under stirring to a 1 M LiOH and 3 M NH_4OH solution leading to a blue–green coprecipitate. An excess of lithium ($Li/(Ni+Al) = 1.05$) was used to compensate for lithium loss during the calcination. Remaining water and ammonia were removed in a rotary evaporator at 80 °C under primary vacuum. Resulting products were dried for 20 h at 110 °C in air; then, they were heated for 5 h at 700 °C ($y = 0.10$) or 750 °C ($0.15 \leq y \leq 0.50$) under a dry oxygen stream. After grinding, the products were heated again, one or two times more at 750−800 °C, under oxygen stream.

Prepared samples were characterized by X-ray diffraction using a Siemens D5000 diffractometer equipped with a diffracted beam monochromator (Cu Kα radiation). Step-scan recordings were carried out in the 10–80° (2θ) range using 0.02° (2θ) steps of 2 s duration for routine characterization or in the 10–120° (2θ) range using 0.02° (2θ) steps of 40 s duration when the XRD pattern is used for Rietveld refinement.

Neutron diffraction data were recorded with the 1.594 Å wavelength on the high resolution powder diffractometer D2B of Institut Laue Langevin (ILL, Grenoble, France). Diffraction patterns were collected at room temperature from 0 to 162° (2θ) with an 0.05° step. Vanadium cans of 8 mm diameter and 5 cm height were used. Due to the geometry of the diffractometer (transmission mode), an absorption correction was required, through the μR factor (μ: linear absorption coefficient for the sample, R: inside radius of the vanadium can), before any structural refinement by the Rietveld method [31].

Magnetic measurements were done with a Superconducting Quantum Interface Device (quantum Design MPMS-5S) at 5 K over the field range of −0.2 to 0.2 T.

Electrochemical properties of $LiNi_{1-y}Al_yO_2$ were examined in lithium cells containing lithium foil as negative electrode. The positive electrodes were prepared by mixing 88 wt.% active material with 10 wt.% of a mixture of carbon black and graphite (1:1) as conductive agent and 2 wt.% polytetrafluoroethylene (PTFE) as binder. The electrolyte used was 1 M $LiPF_6$ dissolved in a mixture of propylene carbonate (PC), ethylene carbonate (EC) and dimethyl carbonate (DMC) (1:1:3 by volume). Cells were assembled in an argon-filled dry box and cycled at room temperature in galvanostatic mode.

Deintercalated phases were obtained through electrochemical charge at a $C/100$ constant rate (corresponding to a theoretical exchange of one electron in 100 h during charge or discharge). The positive electrodes were removed from the cells in a glove box, washed with DMC and then dried under vacuum. XRD patterns were recorded on a Philips diffractometer (PW 1730/10, Cu Kα) in the 5–110° (2θ) range (0.02°/10 s), using a sample holder preventing any contact of the electrode with air.

Scanning electron micrographs were recorded with Hitachi S4500 field emission microscope with an accelerating voltage of 3.0 kV.

3. Structural characterization

Fig. 1 shows the X-ray diffraction patterns of the $LiNi_{1-y}Al_yO_2$ compounds ($0.10 \leq y \leq 0.50$): whatever the aluminum amount, materials isostructural to $LiNiO_2$ are obtained. Extra peaks corresponding to the γ-$LiAlO_2$ phase can be observed for $y = 0.50$, confirming that a solid solution is obtained only in a restricted composition range [11,26,28,32]. This can be explained by the difference in structure between the two limit phases: $LiNiO_2$ has a 2D α-$NaFeO_2$ type structure, whereas γ-$LiAlO_2$ has a γ-$NaFeO_2$

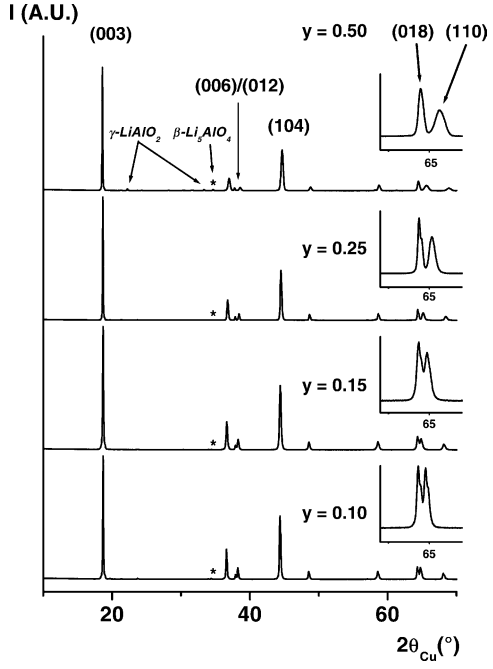

Fig. 1. X-ray diffraction patterns of the $LiNi_{1-y}Al_yO_2$ phases ($y = 0.10$, 0.15, 0.25 and 0.50). Enlargements in the 62–67° (2θ) range are given in inserts. The asterisk (*) shows the more intense diffraction line for β-Li_5AlO_4.

type structure with Al^{3+} and Li^{+} in tetrahedral sites. Note that α-$LiAlO_2$ with the α-$NaFeO_2$ structure is stable only at low temperature (i.e. below 600 °C) [33,34].

Whatever the synthesis temperature and the composition of the material, peaks corresponding to the β-Li_5AlO_4 impurity are observed. Furthermore, traces of Li_2CO_3 are also present due to the use of LiOH in excess for the synthesis.

As shown in Fig. 1, the diffraction lines remain quite narrow for samples with $y \leq 0.25$, indicating good crystallinity of the materials. Nevertheless, the (1 1 0) diffraction line becomes broader (enlargements given in inserts in Fig. 1) whereas the intensity ratio of the (0 1 8)/(1 1 0) peaks remains quite constant (∼0.9) when y increases; that suggests an inhomogeneous distribution of Al^{3+} ions in the structure. The difference in size between nickel and aluminum ions ($r_{Ni^{3+}} = 0.56$ Å and $r_{Al^{3+}} = 0.53$ Å [35]) associated with a Ni^{3+}/Al^{3+} segregation would give rise to a distribution of metal–metal distances and, therefore, to a large broadening of the (1 1 l) diffraction lines. The intensity ratio of the (0 0 3)/(1 0 4) diffraction lines remains quite constant for $y \leq 0.25$: it suggests thus, that substitution of aluminum for nickel does not affect the layered nature of the material. This hypothesis will be confirmed in the following by Rietveld analysis.

Note that no improvement of the $LiNi_{1-y}Al_yO_2$ lamellar character and of the Ni/Al distribution within these materials was obtained using the hydroxide route synthesis (i.e. at first, synthesis of the nickel–aluminum hydroxide and then, high temperature thermal treatment of this hydroxide with the lithium precursor). Furthermore, thermal treatments at higher temperatures were shown to favor lithium loss and, therefore, formation of lithium deficient materials, instead of improving the Ni/Al distribution within the materials.

Refinements by the Rietveld method of the X-ray and neutron diffraction patterns were performed using the Fullprof program [31]. In a first step, refinements of the XRD patterns were realized, assuming a perfectly ordered α-$NaFeO_2$ type structure (R-3m space group) with one Li in the 3b site (0, 0, 1/2), $(1 - y)$ Ni and y Al in the 3a site (0, 0, 0) and two O in the 6c site (0, 0, z_{ox}) (z_{ox} being close to 0.25). The site occupancies were fixed while the isotropic atomic displacement parameters (B) were allowed to vary. Negative values were obtained for the B(Li) parameter, showing an excess of electronic density in the lithium site due to the presence of nickel or aluminum ions in the interslab space [7]. In a second step, a partial occupancy of the lithium site by either nickel or aluminum was thus assumed. Good agreements between the experimental and the calculated diffraction patterns were obtained in both cases: for instance, for $LiNi_{0.85}Al_{0.15}O_2$, 5.5(4)% Ni or 9(2)% Al were found to be present in the 3b lithium site. Note that whatever the structural model considered, none of them enables to fit the asymmetry of the (0 1 8)/(1 1 0) doublet lines.

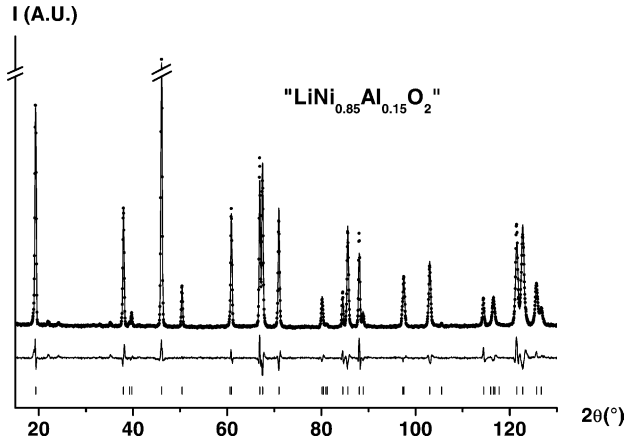

Fig. 2. Comparison of the experimental (●) and calculated (–) neutron diffraction patterns for the $LiNi_{0.85}Al_{0.15}O_2$ phase. The 130–160° (2θ) range is not represented to enlarge the figure.

In order to precise the cationic distribution and especially to check the presence or not of extra-lithium atoms in the 3a site, neutron diffraction was done on the $LiNi_{0.85}Al_{0.15}O_2$ compound. The difference in Fermi length for nickel and aluminum atoms (1.03×10^{-12} and 0.34×10^{-12} cm, respectively) was not sufficient to clearly determine the nature of the cation present in the lithium site, as it was done for the $LiNi_{1-y}Ti_yO_2$ system [36]. Indeed, the ratio of the Fermi lengths (∼3) is close to the ratio of the number of electrons (∼2.6). Good agreements between the experimental and the calculated neutron diffraction patterns were obtained with both hypotheses, i.e. by considering either nickel or aluminum ions in the interslab space. 4.0(6)% Ni or 8(2)% Al were found to be present in the lithium site, in good agreement with the values found by XRD. Fig. 2 and Table 1 present the results obtained in the case of extra-nickel ions in the lithium site. Note that the hypothesis with extra-lithium atoms in the 3a site to compensate for extra-nickel (or aluminum) ions in the 3b lithium site leads to elevated $B(Li)_{3b}$ parameter (3.3(2) $Å^2$), without improving the reliability factors. The possibility of a Li/Ni(Al) mixing between the 3a and 3b sites was, therefore, excluded. Furthermore, on the contrary to what was observed by XRD and NMR by Stoyanova et al. [37] for $LiNi_{1-y}Al_yO_2$ and $LiCo_{1-y}Al_yO_2$ systems, Fourier maps performed using the neutron diffraction data, did not show residual nuclear density in the tetrahedral sites of the slab or of the interslab space. It should be noted that the $LiCo_{1-y}Al_yO_2$ system was recently revisited by the same authors by ^{7}Li, ^{27}Al and ^{59}Co NMR; they showed that aluminum is in effect not present in tetrahedral site [38]. Besides, Yoon et al. [39] have also obtained, by Rietveld refinement of the $LiCo_{1-y}Al_yO_2$ neutron diffraction patterns, a negative occupation ratio for aluminum on tetrahedral site.

Magnetization hysteresis loops were recorded at 5 K versus the magnetic field, in order to find out the possible existence of ferromagnetic interactions in these $LiNi_{1-y}Al_yO_2$ materials. As shown in Fig. 3, a comparison of the $LiNi_{0.85}Al_{0.15}O_2$

Table 1
Parameters and reliability factors obtained by the Rietveld refinement of the $LiNi_{0.85}Al_{0.15}O_2$ neutron diffraction pattern[a]

	Site	Wyckoff positions	Occupancy	B (Å^2)
Li (1)	3b	(0, 0, 1/2)	0.960(5)	2.3(6)
Ni (1)	3b	(0, 0, 1/2)	0.040(5)	2.3(6)
Ni (2)	3a	(0, 0, 0)	0.844(5)	0.47(5)
Al (1)	3a	(0, 0, 0)	0.156(5)	0.47(5)
O (1)	6c	(0, 0, z_{ox} = 0.2588(2))	1	0.92(9)

$Li_{1-z}(Ni_{0.85}Al_{0.15})_{1+z}O_2$

Crystal details	Constraints
Space group: R-3m	$n(Li)_{3b} + n(Ni)_{3b} = 1$
a_{hex}: 2.87022(3) Å	$n(Ni)_{3a} + n(Al)_{3a} = 1$
c_{hex}: 14.2228(1) Å	$n(Al)_{3a}/(n(Ni)_{3a} + n(Ni)_{3b}) = 15/85$
	$B(Li)_{3b} = B(Ni)_{3b}$
	$B(Al)_{3a} = B(Ni)_{3a}$
Conditions of the run	**Profile parameters**
Temperature: 300 K	Pseudo-Voigt function: PV = ηL + (1 − η)G with $\eta = \eta_0 + X(2\theta)$, $\eta_0 = 0.26(2)$; $X = 0$
Angular range: $-7.45^\circ \le 2\theta \le 162^\circ$	Half-width parameters: $U = 0.162(8)$; $V = -0.14(2)$; $W = 0.130(7)$
Number of points: 3390	
Zero point (2θ): 0.009(3)°	
Number of fitted parameters: 15	

Conventional Rietveld R-factors for points with Bragg contribution: $R_{wp} = 14.1\%$; $R_B = 3.15\%$

[a] The standard deviations were multiplied by the Scor parameter (=2.77) to correct for local correlations [31].

hysteresis loop is made with the ones recorded for $(Li_{0.94}Ni_{0.06})NiO_2$ and $(Li_{0.98}Ni_{0.02})NiO_2$, that are characterized by the presence of 6 and 2% of extra-Ni^{2+} ions in the lithium site, respectively. The residual magnetization observed for a zero magnetic field shows the presence of ferromagnetic interactions due to the formation of ferrimagnetic clusters resulting from the presence of paramagnetic ions in the interslab space [40–44]. The Al^{3+} ions being diamagnetic, these measurements confirm thus the presence of extra-nickel ions in the interslab space for the $LiNi_{1-y}Al_yO_2$ materials. As shown in Fig. 4, the thermal variations of the reciprocal molar susceptibility for $LiNi_{0.85}Al_{0.15}O_2$ is similar to that reported for $Li_{0.98}Ni_{1.02}O_2$: it is characteristic of a Curie–Weiss paramagnetic type

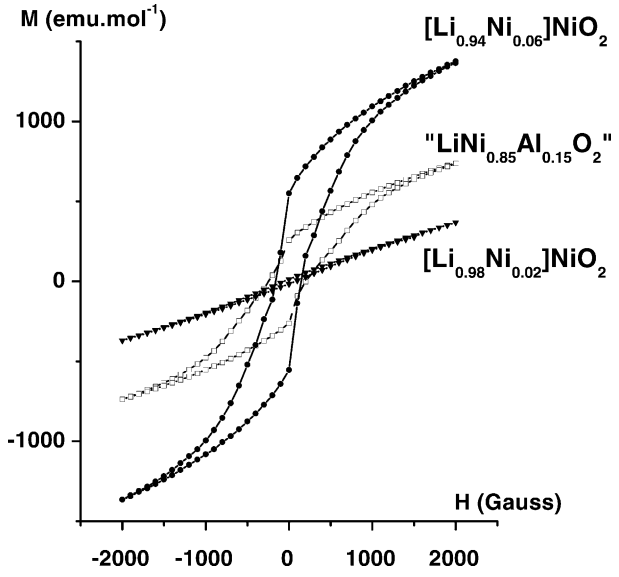

Fig. 3. Comparison of the hysteresis loops recorded at 5 K vs. magnetic field for $Li_{0.94}Ni_{1.06}O_2$, $Li_{0.98}Ni_{1.02}O_2$ and $LiNi_{0.85}Al_{0.15}O_2$.

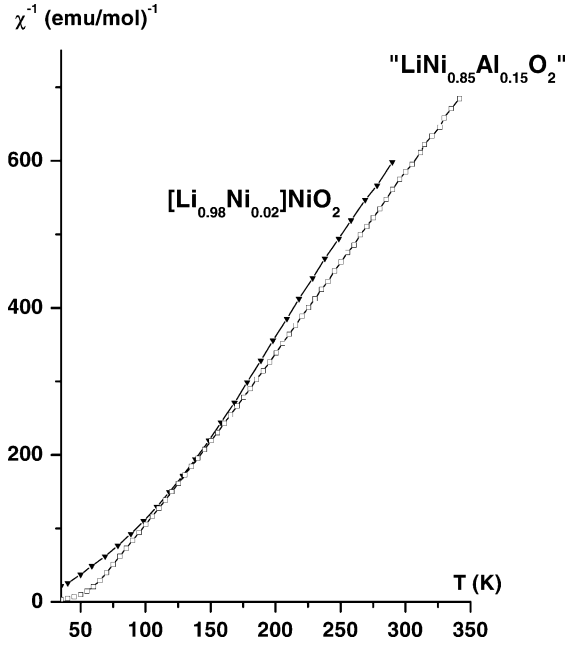

Fig. 4. Comparison of the thermal evolution of the inverse molar magnetic susceptibility for $Li_{0.98}Ni_{1.02}O_2$ and $LiNi_{0.85}Al_{0.15}O_2$ (applied field = 1.8 T).

Table 2
Structural parameters, nickel average oxidation states, crystallographic formulas and reliability factors determined by the Rietveld refinement of the X-ray and neutron diffraction data of the $LiNi_{1-y}Al_yO_2$ phases ($0 \leq y \leq 0.50$)

y in $LiNi_{1-y}Al_yO_2$	a_{hex} (Å)	c_{hex} (Å)	z_{ox}	$S_{(MO_2)}$ (Å)[a]	$I_{(LiO_2)}$ (Å)[b]	Ni average oxidation number	Crystallographic formula	R_{wp} (%)	R_B (%)
0	2.8766(4)	14.211(7)	0.2596(6)	2.10(2)	2.64(2)	2.96	$[Li_{0.98}Ni^{II}_{0.02}][Ni^{III}_{0.98}Ni^{II}_{0.02}]O_2$	12.1	2.17
0.10	2.87494(4)	14.2187(2)	0.2582(5)	2.14(1)	2.60(1)	2.89	$[Li_{0.947}Ni^{II}_{0.053}]$ $[Ni^{III}_{0.842}Ni^{II}_{0.053}Al_{0.105}]O_2$	11.3	1.94
0.15	2.87035(4)	14.2223(2)	0.2586(4)	2.13(1)	2.61(1)	2.88	$[Li_{0.945}Ni^{II}_{0.055}]$ $[Ni^{III}_{0.787}Ni^{II}_{0.055}Al_{0.158}]O_2$	11.2	2.45
0.25	2.86081(4)	14.2331(2)	0.2590(5)	2.11(1)	2.63(1)	2.89	$[Li_{0.957}Ni^{II}_{0.043}]$ $[Ni^{III}_{0.696}Ni^{II}_{0.043}Al_{0.261}]O_2$	13.3	2.65
0.50	2.84150(5)	14.2504(4)	0.2599(7)	2.09(2)	2.66(2)	2.81	$[Li_{0.951}Ni^{II}_{0.049}]$ $[Ni^{III}_{0.427}Ni^{II}_{0.049}Al_{0.524}]O_2$	18.7	4.40

[a] Slab thickness: $S(MO_2) = 2[(1/3) - z_{ox}]c_{hex}$.
[b] Interslab space thickness: $I(LiO_2) = (c_{hex}/3) - S(MO_2)$.

behavior above 100 K. The experimental Curie constant ($C_{exp} = 0.42$) is in quite good agreement with the spin only calculated one ($C_{theor} = 0.40$) assuming the $[Li_{0.95}Ni^{II}_{0.05}]_{3b}$-$[Ni^{II}_{0.05}Ni^{III}_{0.79}Al_{0.16}]_{3a}O_2$ cationic distribution for $LiNi_{0.85}$-$Al_{0.15}O_2$, the trivalent nickel ions being in the classical low spin configuration.

Magnetic measurements have shown the presence of extra-nickel ions in the lithium site. Moreover, the formation of the $LiMO_2$-type structure results from the difference in size between the LiO_6 and MO_6 octahedra. Therefore, by just taking into account the difference in size between the different cations, the aluminum ions were expected to preferentially occupy the nickel site ($r_{L^+} = 0.74$ Å, $r_{Ni^{2+}} = 0.70$ Å, $r_{Ni^{3+}} = 0.56$ Å and $r_{Al^{3+}} = 0.53$ Å). The following cationic distribution is thus proposed for $LiNi_{1-y}Al_yO_2$ materials: $[Li_{1-z}Ni^{II}_z]_{3b}[Ni^{II}_zNi^{III}_{1-t-z}Al_t]_{3a}O_2$ with $t = y(1 + z)$. About 5% of extra-nickel ions were found in the lithium site for all compounds, whatever the aluminum content (Table 2).

The asymmetry of the (0 1 8)/(1 1 0) doublet lines experimentally observed by X-ray and neutron diffraction could be explained by short range inhomogeneity, such as a tendency to aluminum clustering; this effect can not be taken into account by the pattern Rietveld refinement that gives only an average structure. Indeed, an inhomogeneity of the cationic distribution in specific planes in a structure induces locally slight modifications of the atomic positions, that lead to a distribution of d-spacing distances and, therefore, to the broadening of some specific diffraction lines.

As shown in Fig. 1, upon increasing aluminum content, the (1 1 0) peak shifts toward higher 2θ angles while the (0 0 6) and (0 1 8) peaks shift toward lower 2θ angles, resulting in a larger splitting of (0 0 6)/(0 1 2) and (0 1 8)/(1 1 0) diffraction lines. Substitution of aluminum for nickel results thus in shorter a_{hex} and larger c_{hex}, increasing the c_{hex}/a_{hex} ratio (Fig. 5). In the layered $LiNiO_2$ derivatives, the cell parameter variation when a L cation is substituted for nickel depends on several contribution: (i) the size of the L^{n+} cation versus the trivalent nickel one, (ii) the charge of the L^{n+} cation that can induce a change in the oxidation state of nickel ions, (iii) the amount of extra-nickel ions (Ni^{2+}) in the lithium site that tend to link the slabs, (iv) the (Ni,L)–O covalency that is directly related to the difference in ionicity of the bonds. While the variation of the a parameter can be directly discussed from the previous points, in the case of the c parameter one has to consider separately the slab thickness (S) and the interslab thickness (I) that can vary in opposite directions upon cationic substitution.

In the case of the aluminum-substituted lithium nickelates, the following observations were made:

- Concerning the a_{hex} parameter, one has essentially to consider the difference in ionic radii between Ni^{3+}, Al^{3+} and Ni^{2+} ($r_{Ni^{3+}} = 0.56$ Å, $r_{Al^{3+}} = 0.53$ Å and $r_{Ni^{2+}} = 0.70$ Å). As shown in Fig. 5, at the very beginning of the substitution, the decrease expected from the presence of aluminum is compensated by the presence of 5% of Ni^{2+} in the slab. For larger substitution amounts, the observed decrease results from the lower size of aluminum since the amount of Ni^{2+} remains constant.

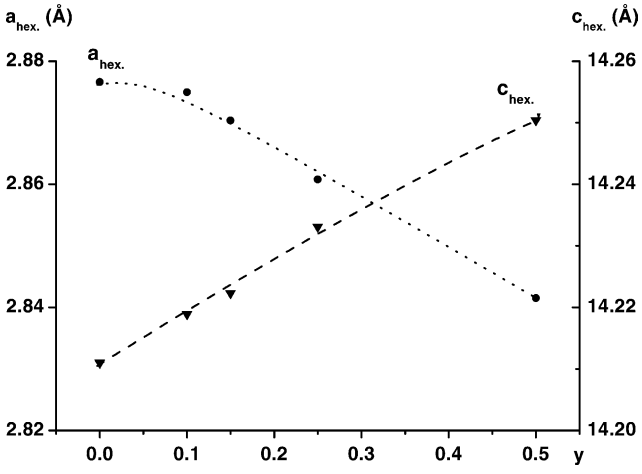

Fig. 5. Variation vs. y of the a_{hex} and c_{hex} cell parameters for the $LiNi_{1-y}Al_yO_2$ phases.

- As shown in Table 2, the slab thickness (S) increases at the very beginning of the substitution (presence of 5% of Ni^{2+} in the slab) and then decreases (increasing amount of small Al^{3+} ions). The interslab thickness (I) varies in the opposite way: the decrease at the beginning of the substitution results from the presence of 5% of Ni^{2+} in the lithium site, while the small increase observed for larger substitution amount results from the increasing repulsion between the slabs due to the ionic character of the Al–O bonds. As far as the c_{hex} parameter is concerned, the variations of S and I almost compensate leading to a small increase of the c_{hex} parameter, that in relative value is five times lower than the decrease of the a_{hex} parameter (Fig. 5).

4. Electrochemical study

A general electrochemical study was carried out to determine the effects of aluminum substitution on the electrochemical behavior of the $Li_xNi_{1-y}Al_yO_2$ materials ($y = 0$, 0.10, 0.15 and 0.25) as positive electrode materials for lithium batteries. In the following, the true crystallographic formula deduced for these materials from the analysis of their X-ray and neutron diffraction patterns by Rietveld refinement will be used. The cycling tests were done at a constant $C/20$ rate in the 3–4.15 V range. Fig. 6a–d shows the variation of cell voltage versus lithium composition during the first 10 cycles for $Li_{0.98}Ni_{1.02}O_2$ ($y = 0$), $Li_{0.95}Ni_{0.95}Al_{0.10}O_2$ ($y = 0.10$), $Li_{0.95}Ni_{0.89}Al_{0.16}O_2$ ($y = 0.15$) and $Li_{0.96}Ni_{0.78}Al_{0.26}O_2$ ($y = 0.25$). Good cycling stability is observed for $y \leq 0.15$. The average reversible capacities are quite good for $y \leq 0.15$ (higher than 120 Ah kg^{-1}) but tend to decrease with increasing y due to the electrochemical inactivity of aluminum ions during the redox process. A quite high irreversible capacity is observed (~50 Ah kg^{-1}) at the end of the first discharge for each aluminum substituted lithium nickelate. This can be explained by the presence of about 5% extra-nickel ions in the interslab space, whatever the aluminum content. Indeed, the irreversible oxidation of these extra-nickel ions during the first charge induces local collapses in the interslab space and, therefore, hinders afterwards a good diffusion of the lithium ions in the structure and, therefore, the reintercalation of Li

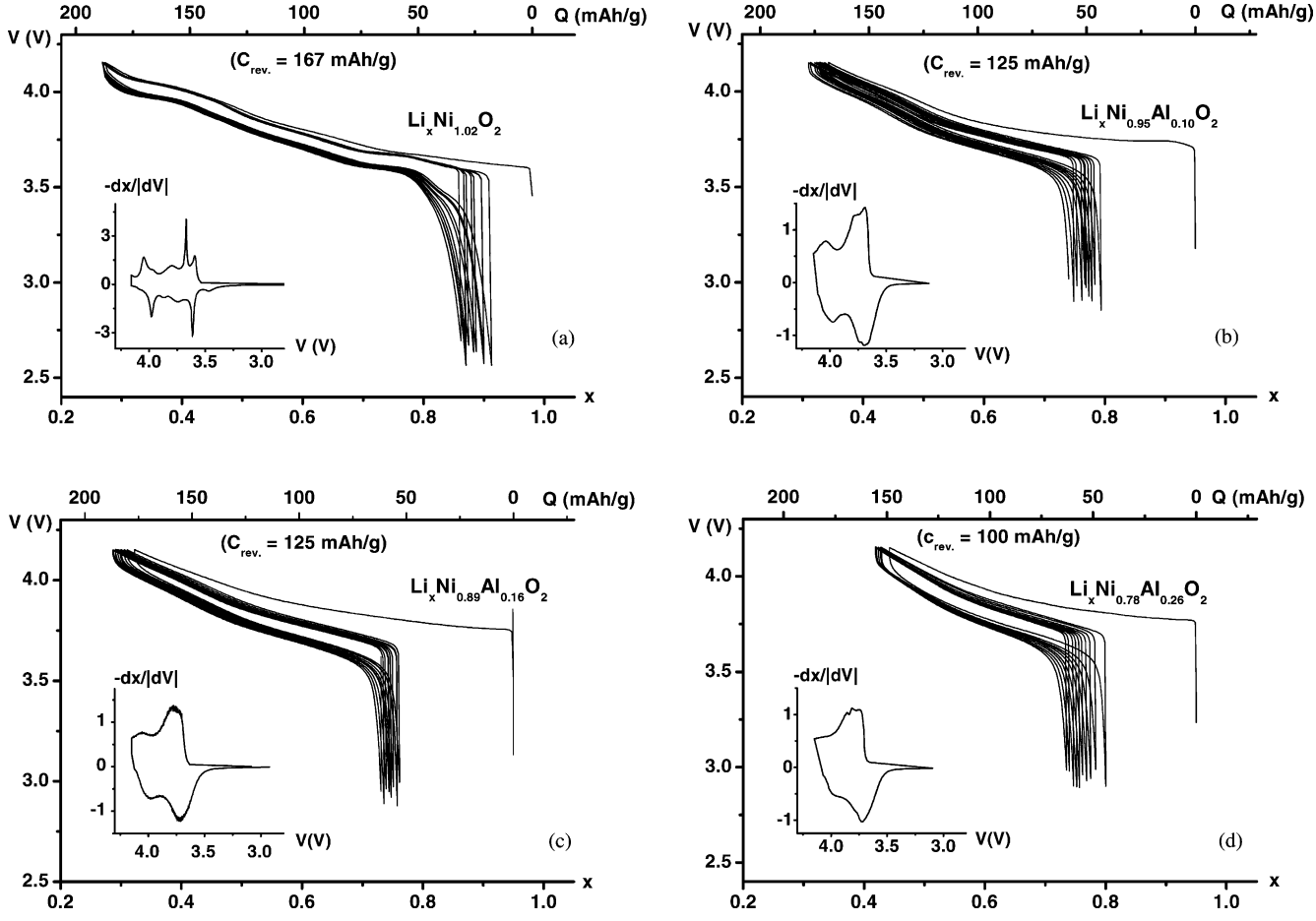

Fig. 6. Variation of the cell voltage vs. lithium amount at the $C/20$ rate for the first ten galvanostatic charge/discharge cycles of Li//$Li_xNi_{1-y}Al_yO_2$ cells ($y = 0$ (a), $y = 0.10$ (b), $y = 0.15$ (c), $y = 0.25$ (d)). The average reversible specific capacity over 10 cycles is specified for each cell. The $-dx/|dV| = f(V)$ incremental capacity curves versus voltage are given in inserts.

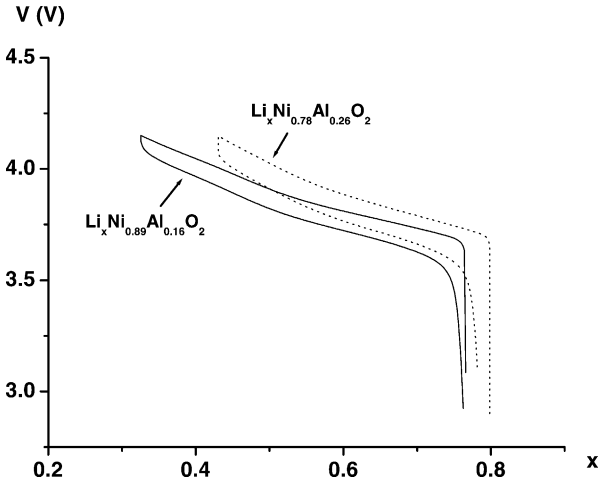

Fig. 7. Comparison of the second charge–discharge cycle obtained at the *C*/20 rate for Li//$Li_xNi_{0.89}Al_{0.16}O_2$ and Li//$Li_xNi_{0.78}Al_{0.26}O_2$ cells.

ions in their vicinity [8]. Note also that an increase of the polarization is observed when the aluminum content increases. This can be explained by the fact that aluminum ions disturb the charge delocalization within the slab and, therefore, the Li^+ ions diffusion in the structure. The second charge and discharge cycles of Li//$Li_xNi_{1-y}Al_yO_2$ batteries are compared in Fig. 7. An increase of the average potential of the battery is observed with increasing aluminum substitution for nickel, in good agreement with the ab initio calculations performed by Ceder et al. [46] and Ceder and coworkers [45,47] for $LiCo_{1-y}Al_yO_2$ and with experimental results obtained for instance by Ohzuku and Nakura [48], Ohzuku et al. [49], and by Zhong and Von Sacken [32] for the $LiNi_{1-y}Al_yO_2$ system.

On the contrary to what is observed for the Li//Li_xNiO_2 system, derivative curves $-dx/|dV| = f(V)$ do not exhibit any sharp peak corresponding to a plateau in the cell voltage versus lithium composition curve (Fig. 6a–d). Therefore, it can be assumed that no structural first order phase transition occurs during cycling.

As it can be seen in Fig. 8, charge curves obtained for deintercalation of various lithium amounts from $Li_xNi_{0.89}Al_{0.16}O_2$ superpose very well, indicating a good reproducibility of the results. The evolution of the XRD patterns with decreasing lithium content shows continuous displacements of the peaks (Fig. 9). The structure remains similar to that observed for the starting $Li_{0.95}Ni_{0.89}Al_{0.16}O_2$ material and can thus be indexed in the *R*-3*m* space group. No phase transition is observed, confirming the existence of a solid solution through the 0.05–0.95 lithium range. It is interesting to note that the $[Li_{0.95}Ni^{II}_{0.05}][Ni^{II}_{0.05}Ni^{III}_{0.79}Al_{0.16}]O_2$ cationic distribution allows to theoretically remove 0.94 Li^+ ions from $Li_{0.95}Ni_{0.89}Al_{0.16}O_2$, assuming the oxidation of the nickel ions of the slab to the tetravalent state and those of the interslab space to the trivalent state [8,9]. The experimental results have shown that 0.90 Li^+ ions can be removed from the structure (within the uncertainty due to electrolyte decomposition at high voltage); they are, therefore, in really good agreements with the cationic distribution deduced from the diffraction analysis for $Li_{0.95}Ni_{0.89}Al_{0.16}O_2$.

The existence of a solid solution through the 0.05–0.95 lithium range confirms that partial aluminum substitution for nickel ($y \geq 0.10$) prevents the phase transitions observed for the Li_xNiO_2 system, which are associated with lithium/vacancy orderings in the interslab space and charge (Ni^{3+}/Ni^{4+}) orderings in the slab [11,26,28,50,51]. The disappearance of the phase transitions occurs more or less rapidly, depending on the substituting cations (Co [52], Fe [53], Mg [54], etc.). In the case of the aluminum substituted materials, a small amount of aluminum substitution is sufficient to suppress all the phase transitions. Indeed, the presence of ~5% of extra-nickel ions whatever the aluminum content and also the existence of local inhomogeneities such as nickel/aluminum segregation hinder the formation of the Li/vacancy orderings in the interslab space.

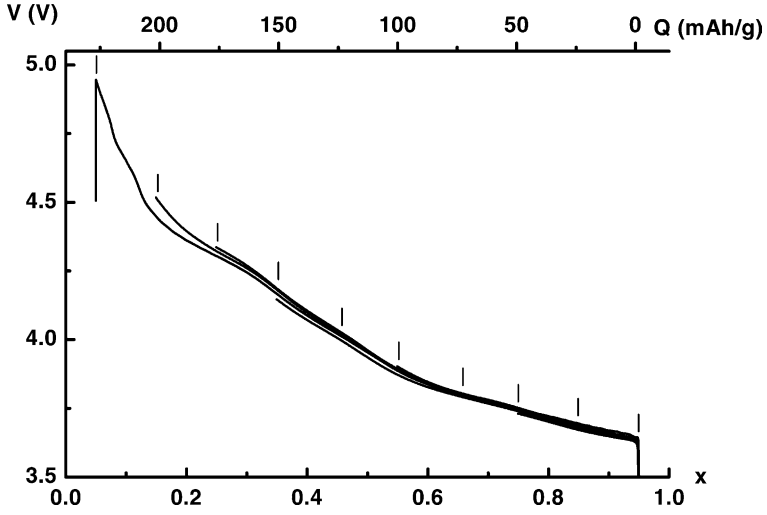

Fig. 8. Charge curves of Li//$Li_xNi_{0.89}Al_{0.16}O_2$ cells obtained at the *C*/100 rate.

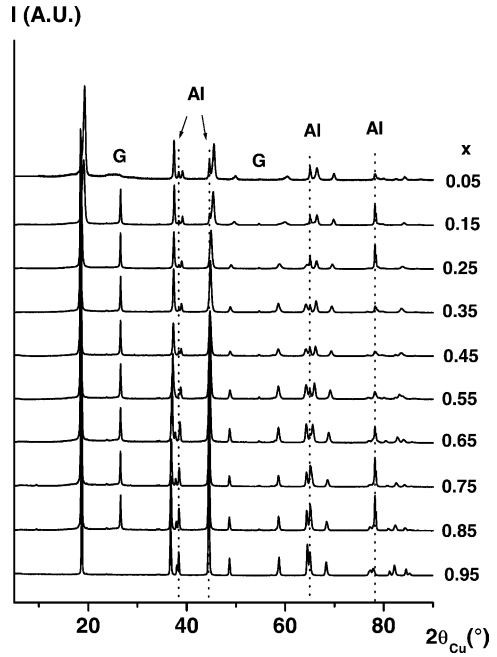

Fig. 9. X-ray diffraction patterns of the $Li_xNi_{0.89}Al_{0.16}O_2$ deintercalated phases (G: graphite, Al: sample holder).

Enlargements in the 17–21° (2θ) and 60–67.5° (2θ) ranges show in Fig. 10, a displacement to higher diffraction angle and a severe broadening of the (0 0 3) and (0 1 8) lines when x becomes smaller than 0.35. The displacement to higher diffraction angle, previously observed for Li_xNiO_2 and $Li_xNi_{1-y}Mg_yO_2$ systems [54,55], goes with the decrease of the interlayer distance at the end of the charge. As shown in Fig. 11, the variation as a function of decreasing x, of the cell parameters a_{hex} and c_{hex} deduced from the 'full pattern

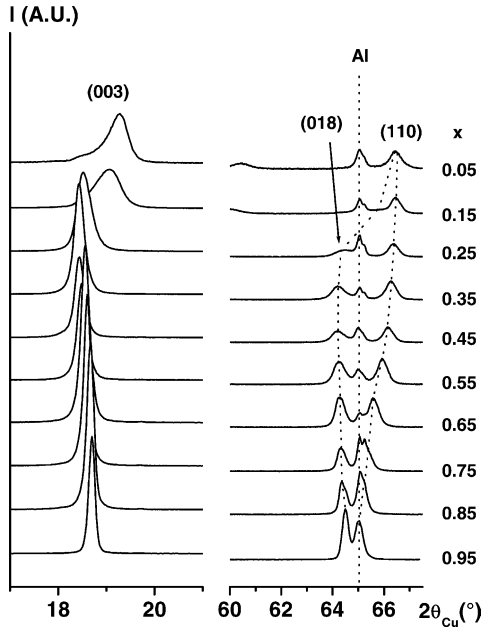

Fig. 10. Enlargements in the 17–21° (2θ) and 60–67.5° (2θ) ranges of the $Li_xNi_{0.89}Al_{0.16}O_2$ deintercalated phase XRD patterns.

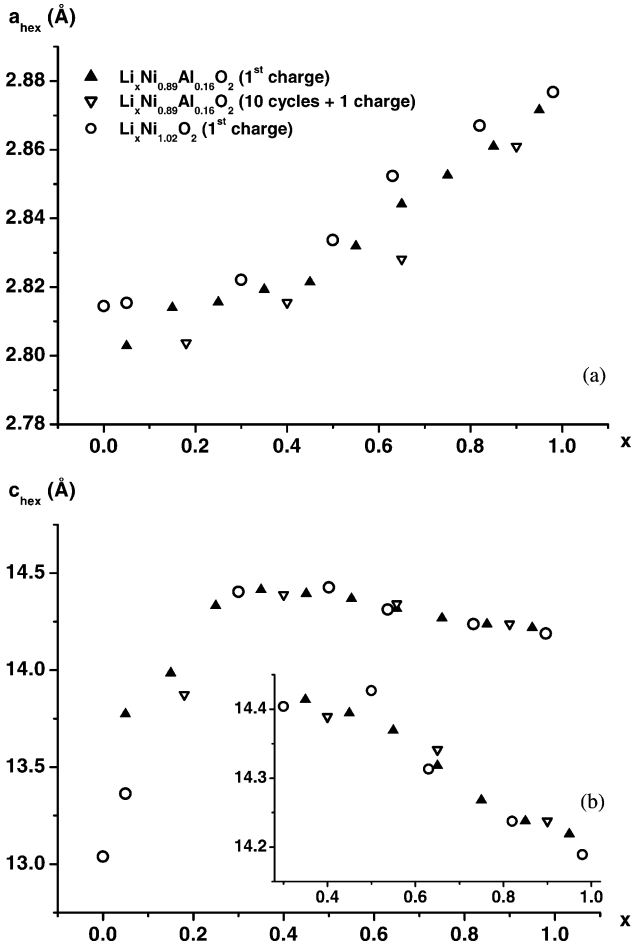

Fig. 11. Variation of a_{hex} (a) and c_{hex} (b) vs. lithium amount (x) for the $Li_xNi_{0.89}Al_{0.16}O_2$ phases, obtained during the first charge cycle and after 10 cycles plus 1 charge cycle, in comparison to the ones observed for the $Li_xNi_{1.02}O_2$ system.

matching' refinement of the XRD patterns, is quite similar to that observed for the Li_xNiO_2 system. The a_{hex} parameter decreases because of the nickel oxidation. The c_{hex} parameter increases in the 0.35–0.95 lithium composition range due to the increase of the electrostatic repulsions between adjacent oxygen layers through the interslab space. Indeed, Li^+ ions do not play their role of screening ions anymore. For $x < 0.35$, the broadening of the diffraction lines and, especially of the (0 0 l), suggests local inhomogeneities due to fluctuations of the cationic distribution (extra-nickel ions and remaining lithium ions) between the interslab spaces. These inhomogeneities induce local deformations of the interslab thickness that lead to a distribution of interslab distances in the structure and, therefore, to a large broadening of the (0 0 l) diffraction lines. A continuous decrease of the c_{hex} parameter is observed for $x < 0.35$, showing that the structure becomes covalent enough for the steric effects to prevail over the electrostatic ones. Indeed, at the end of the deintercalation, when the amount of tetravalent nickel ions is very large, the Ni(Al)–O bond covalency increases enough to induce a decrease of the charge carried by the oxygen ions

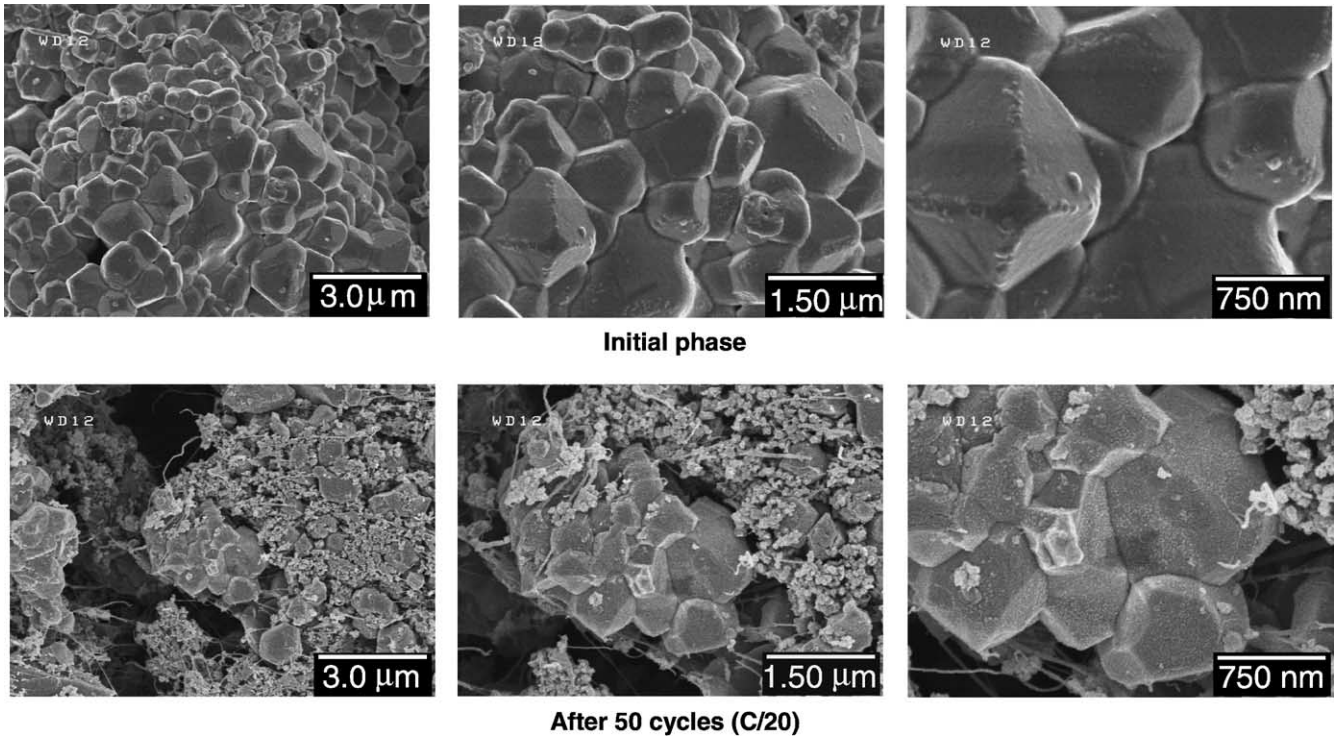

Fig. 12. Scanning electron micrographs obtained for $LiNi_{0.89}Al_{0.16}O_2$ before and after 50 cycles, at the *C*/20 rate in the 3–4.15 V range.

and, therefore, a decrease of the electrostatic repulsions between adjacent oxygen planes, even if the lithium ions do not play their role of screening ions anymore.

The variations of the cell parameters obtained for electrodes, charged after 10 cycles at the *C*/20 rate in the 3–4.15 V range, remain quite similar to that observed during the first charge at the *C*/100 rate (Fig. 11). This result suggests that no cationic migration occurs upon cycling, on the contrary to what was observed in the case of $Li(Ni,Mg)O_2$ system [54].

High resolution scanning electron micrographs were performed for the $LiNi_{1-y}Al_yO_2$ materials to characterize the changes in the crystallites morphology resulting from the electrochemical cycling. Fig. 12 shows the micrographs obtained for $LiNi_{0.89}Al_{0.16}O_2$ before cycling and after 50 cycles at the *C*/20 rate in the 3–4.15 V range (in its reintercalated state). The initial material appears to be composed of aggregates of particles with diameter in the 1 µm range. After 50 cycles, the morphology of the particles remains quite similar. Besides, cohesion between crystallites remains good, showing that structural strains occurring during the cycling are limited in this potential range. These results are very similar to those obtained for $LiNiO_2$ in the same potential range of cycling [56].

5. Conclusion

In this work, a thorough study of the $LiNi_{1-y}Al_yO_2$ system was performed. By Rietveld refinements of X-ray and neutron diffraction data, correlated with magnetic measurements, the cationic distribution was determined to be $[Li_{1-z}Ni^{II}_z]_{3b}[Ni^{II}_zNi^{III}_{1-t-z}Al_t]_{3a}O_2$ with $t = y\ (1 + z)$. About 5% of extra-nickel ions were found in the interslab space for all compounds. Cycling tests showed that 10% aluminum is sufficient to suppress all the phase transitions observed for the Li_xNiO_2 system. A good cyclability is obtained; nevertheless, a decrease of the reversible capacity and an increase of the polarization were observed when *y* increases. Morphology and cohesion between crystallites remain the same after 50 cycles at the *C*/20 rate in the 3–4.15 V range, showing that structural strains are limited during cycling.

Acknowledgements

The authors wish to thank J.P. Pérès, P. Biensan and M. Broussely for fruitful discussions, E. Suard and Institut Laue Langevin (Grenoble, France) for neutron diffraction, C. Denage for technical assistance, Saft and Région Aquitaine for financial support.

References

[1] M.G.S.R. Thomas, W.I.F. David, J.B. Goodenough, P. Groves, Mater. Res. Bull. 20 (1985) 1137.
[2] J.R. Dahn, U. Von Sacken, M.W. Juzkow, H. Al-Janaby, J. Electrochem. Soc. 138 (8) (1991) 2207.
[3] M. Broussely, F. Perton, J. Labat, R.J. Staniewicz, A. Romero, J. Power Sources 43–44 (1993) 209.

[4] T. Ohzuku, A. Ueda, Solid State Ionics 69 (1994) 201.
[5] M. Broussely, F. Perton, P. Biensan, J.M. Bodet, J. Labat, A. Lecerf, C. Delmas, A. Rougier, J.P. Pérès, J. Power Sources 54 (1995) 109.
[6] R. Kanno, H. Kubo, Y. Kawamoto, T. Kamiyama, F. Izumi, Y. Takeda, M. Takano, J. Solid State Chem. 110 (1994) 216.
[7] A. Rougier, P. Gravereau, C. Delmas, J. Electrochem. Soc. 143 (4) (1996) 1168.
[8] J.P. Pérès, C. Delmas, A. Rougier, M. Broussely, F. Perton, P. Biensan, P. Willmann, J. Phys. Chem. Solids 57 (1996) 1057.
[9] C. Delmas, J.P. Pérès, A. Rougier, A. Demourgues, F. Weill, A. Chadwick, M. Broussely, F. Perton, P. Biensan, P. Willmann, J. Power Sources 68 (1997) 120.
[10] J.R. Dahn, E.W. Fuller, M. Obrovac, U. Von Sacken, Solid State Ionics 69 (1994) 265.
[11] T. Ohzuku, A. Ueda, M. Kouguchi, J. Electrochem. Soc. 142 (12) (1995) 4033.
[12] H. Arai, S. Okada, Y. Sakurai, J. Yamaki, Solid State Ionics 109 (1998) 295.
[13] C. Delmas, I. Saadoune, Solid State Ionics 53–56 (1992) 370.
[14] C. Delmas, I. Saadoune, A. Rougier, J. Power Sources 43–44 (1993) 595.
[15] E. Zhecheva, R. Stoyanova, Solid State Ionics 66 (1993) 143.
[16] A. Ueda, T. Ohzuku, J. Electrochem. Soc. 141 (8) (1994) 2010.
[17] A. Rougier, I. Saadoune, P. Gravereau, P. Willmann, C. Delmas, Solid State Ionics 90 (1996) 83.
[18] C. Pouillerie, F. Perton, P. Biensan, J.P. Pérès, M. Broussely, C. Delmas, J. Power Sources 96 (2001) 293.
[19] Y. Nishida, K. Nakane, T. Satoh, J. Power Sources 68 (2) (1997) 561.
[20] Y. Sato, T. Koyano, M. Mukai, K. Kobayakawa, Denki Kagaku 66 (12) (1998) 1215.
[21] T. Ohzuku, T. Yanagawa, M. Kouguchi, A. Ueda, J. Power Sources 68 (1) (1997) 131.
[22] H. Arai, S. Okada, Y. Sakurai, J. Yamaki, J. Electrochem. Soc. 144 (9) (1997) 3117.
[23] P. Novak, R. Nesper, M. Coluccia, F. Joho, A. Piotto Piotto, Extended Abstracts of the Lithium Battery Discussion, Electrode Materials, Arcachon, France, 2001.
[24] S.H. Chang, S. Kang, S. Song, J. Yoon, J. Choy, Solid State Ionics 86–88 (1996) 171.
[25] Y. Gao, M.V. Yakovleva, W.B. Ebner, Electrochem. Solid-State Lett. 1 (3) (1998) 117.
[26] A. Rougier, Thesis, University of Bordeaux I, 1995.
[27] Q. Zhong, U. Von Sacken, J. Power Sources 54 (1995) 221.
[28] G.X. Wang, S. Zhong, D.H. Bradhurst, S.X. Dou, H.K. Liu, Solid State Ionics 116 (1999) 271.
[29] S.H. Park, K.S. Park, Y.K. Sun, K.S. Nahm, Y.S. Lee, M. Yoshio, Electrochim. Acta 46 (2001) 1215.
[30] D. Caurant, N. Baffier, B. Garcia, J.P. Pereira-Ramos, Solid State Ionics 91 (1996) 45.
[31] J. Rodriguez-Carvajal, Laboratoire Léon Brillouin (CEA-CNRS), http://www-llb.cea.fr/fullweb/powder.htm.
[32] Q. Zhong, U. Von Sacken, Extended Abstracts of Seventh International Meeting on Lithium Batteries, Boston, MA, 1994, p. 312.
[33] H.-A. Lehmann, H. Hesselbarth, Zeitchrift für anorganische und allgemeine Chemie 313 (1961) 117.
[34] M. Marezio, J.P. Remeika, J. Chem. Phys. 44 (8) (1966) 3143.
[35] R.D. Shannon, C.T. Prewitt, Acta Crystallogr. B25 (1969) 925.
[36] L. Croguennec, E. Suard, P. Willmann, C. Delmas, Chem. Mater. 14 (2002) 2149.
[37] R. Stoyanova, E. Zhecheva, E. Kuzmanova, R. Alcantara, P. Lavela, J.L. Tirado, Solid State Ionics 128 (2000) 1.
[38] E. Gaudin, F. Taulelle, R. Stoyanova, E. Zhecheva, R. Alcantara, P. Lavela, J.L. Tirado, J. Phys. Chem. B 105 (2001) 8081.
[39] W.-S. Yoon, K.-K. Lee, K.-B. Kim, J. Power Sources 97–98 (2001) 303.
[40] A. Rougier, C. Delmas, G. Chouteau, J. Phys. Chem. Solids 57 (1996) 1101.
[41] T. Shirakami, M. Takematsu, A. Hirano, R. Kanno, K. Yamaura, M. Takano, T. Atake, Mater. Sci. Eng. B 54 (1998) 70.
[42] A.L. Barra, G. Chouteau, A. Stepanov, A. Rougier, C. Delmas, Euro. Phys. J. B 7 (4) (1999) 551.
[43] J.N. Reimers, J.R. Dahn, J.E. Greedan, C.V. Stager, G. Liu, I. Davidson, U. Von Sacken, J. Solid State Chem. 102 (1993) 542.
[44] D. Mertz, Y. Ksari, F. Celestini, J.M. Debierre, A. Stepanov, C. Delmas, Phys. Rev. B 61 (2) (2000) 1240.
[45] M.K. Aydinol, A.F. Kohan, G. Ceder, K. Cho, J. Joannopoulos, Phys. Rev. B 56 (3) (1997) 1354.
[46] G. Ceder, Y.M. Chiang, D.R. Sadoway, M.K. Aydinol, Y.I. Jang, B. Huang, Nature 392 (1998) 694.
[47] Y.I. Jang, B. Huang, H. Wang, G.R. Maslkaly, G. Ceder, D.R. Sadoway, Y.M. Chiang, H. Liu, H. Tamura, J. Power Sources 81–82 (1999) 589.
[48] T. Ohzuku, K. Nakura, Denki Kagaku 66 (12) (1998) 1209.
[49] T. Ohzuku, K. Nakura, T. Aoki, Electrochim. Acta 45 (1–2) (1999) 151.
[50] J.P. Pérès, F. Weill, C. Delmas, Solid State Ionics 116 (1–2) (1999) 19.
[51] M.E. Arroyo de Dompablo, C. Marianetti, A. Van der Ven, G. Ceder, Phys. Rev. B 63 (2001) 144107.
[52] I. Saadoune, C. Delmas, J. Mater. Chem. 6 (2) (1996) 193.
[53] G. Prado, A. Rougier, L. Fournès, C. Delmas, J. Electrochem. Soc. 147 (8) (2000) 2880.
[54] C. Pouillerie, L. Croguennec, C. Delmas, Solid State Ionics 132 (2000) 15.
[55] T. Ohzuku, A. Ueda, M. Nagayama, J. Electrochem. Soc. 140 (7) (1993) 1862.
[56] J. P. Pérès, Thesis, University of Bordeaux I, 1996.